Analyses of Electrode Heat Transfer in Gas Metal Arc Welding

In-depth investigation offers insight into the practicality of modeling the GMAW process

BY Y.-S. KIM, D. M. McELIGOT AND T. W. EAGAR

ABSTRACT. Heat and fluid flow in the electrode during gas metal arc welding are considered approximately, experimentally, analytically and numerically for ranges of electrodes and materials of practical importance. Estimation of the governing nondimensional parameters and pertinent time scales provides insight into droplet formation and detachment while demonstrating that the behavior of the solid electrode may be considered to be quasi-steady. The time scale estimates show that a steady-state, spherical flow calculation for the droplet would be inappropriate and possibly misleading. Experimental observations of the formation of a tapering tip, forming as electrical current is increased in steel electrodes shielded by argon gas, are found quantitatively consistent with numerical simulations based on the hypothesis that additional thermal energy is evolved along the cylindrical side surface of the electrode due to electron condensation.

Introduction

Gas metal arc (GMA) welding is the most common method for arc welding steels and aluminum alloys. About 40% of the production welding in this country is accomplished by this process in which the thermal phenomena and melting of the solid electrode are coupled to the plasma arc and the weld pool. Thus, the thermo-fluid behavior of the electrode and detaching drops can have significant effects on the subsequent weld quality and production rate.

While a number of qualitative hypotheses concerning metal transfer have been suggested and in some instances accepted, quantitative proof of their validity is still lacking (Ref. 1). The purpose of the present paper is to provide quantitative analyses, concentrating on the thermal behavior of the electrode, to aid in the fundamental understanding of the process. Main emphasis is on the commercially important application of spray transfer (Refs. 2, 3) from steel electrodes with argon shielding. In particular, it is shown that simple energy balances are inadequate to explain the observed melting phenomena. Instead, heat transfer between the arc and the electrode involves a number of coupled processes. This paper outlines which heat transfer mechanisms predominate and in which regimes each is important.

For a general review of recent work on metal transfer, the reader is referred to Lancaster's chapter in the text by Study Group 212 of the International Institute of Welding (Ref. 4). The pioneering study of metal transfer by Lesnewich (Refs. 2, 3) has been recently summarized by him in a letter (Ref. 5). Cooksey and Miller (Ref. 6) described six modes, and Needham and Carter (Ref. 7) defined the ranges of metal transfer. The axial spray transfer mode is often preferred to ensure maximum arc stability and minimum spatter.

Analyses and experiments have been conducted by Greene (Ref. 8), Halmoy (Ref. 9), Woods (Ref. 10), Ueguri, Hara and Komura (Ref. 11), Allum (Refs. 12, 13) and by Waszink and coworkers (Refs. 14–17). These studies have predominantly addressed steady or static conditions, although Lancaster and Allum did consider transient instabilities for possible explanations of the final stage of the droplet detachment process.

Possible thermal processes that may interact with the forces on the droplet to cause detachment are described schematically in Fig. 1 for an idealized droplet. The process is transient, proceeding from detachment of one droplet through melting, formation and detachment of the next, so there is change in the thermal energy storage, Ṡ. Heating is caused by electrical a resistance heating G and by interaction with the plasma q_p. Heat losses occur via conduction in the solid rod q_k, radiation exchange with the environment q_r, convection to the shielding gas q_c and evaporation at the surface q_v. Internal circulation q_{nc} may be induced by electromagnetic, surface tension, gravity and/or shear forces.

The governing thermal energy equation for the wire and droplet can be written in cylindrical coordinates as (Ref. 18).

$$\frac{\partial \rho I}{\partial t} + \rho u \frac{\partial H}{\partial x} + \rho v \frac{\partial H}{\partial r} = \frac{\partial}{\partial x}\left(kr \frac{\partial T}{\partial x}\right) + \frac{1}{r}\frac{\partial}{\partial r}\left(kr \frac{\partial T}{\partial r}\right) + q_G''' \quad (1)$$

where the dependent variables are the enthalpy (H) and the specific internal thermal energy (I). For steady motion of the solid wire, the radial velocity (v) disappears and the axial velocity (u) is uniform at the wire feed speed V_w. The volumetric thermal energy generation rate (q_G''') is a consequence of resistive (or Joulean) heating. If the boundary conditions and other quantities can also be idealized as steady in time, then the first term (representing transient thermal energy storage) also disappears.

For the droplet, these idealizations are not valid. The velocity field must be determined from the solution of the continuity and momentum equations after solving Maxwell's electromagnetic field equations to obtain body force terms. The droplet grows so the process is nonsteady

KEY WORDS

Gas Metal Arc Welding
Electrode Heat
Heat Transfer
Electron Condensation
Numerical Simulation
Time-Scale Estimates
Tapering Tip
Thermocapillary Flow
Thermal Energy Flow
Nondimension Bond No.

Y.-S. KIM is a Research Associate, Materials Science and Engineering, University of Florida, Gainesville, Fla. D. M. McELIGOT is with Westinghouse Naval Systems Division, Cleveland, Ohio. T. W. EAGAR is a Professor, Materials Science and Engineering, Massachusetts Institute of Technology, Cambridge, Mass.

and the transient terms must be retained (as they might be for the solid wire, since the melting interface also must be affected by the transient droplet). Boundary conditions for the momentum equations include treatment of the surface tension forces that can be dominant. Solution for the droplet fields is thus much more difficult than analysis of the thermal behavior of the solid wire and is beyond the scope of the present work.

The present study examines the thermal processes occurring in moving electrodes for GMAW with the objectives of 1) determining which phenomena are important in controlling the melting rate and 2) explaining the formation of a tapering tip observed for some combinations of electrode materials and shielding gases.

Nondimensional Parameters and Time Scales

Determination of the nondimensional parameters and relative time scales helps to quantify which thermofluid effects are important for which transfer mode. It further provides part of the nondimensional description, which will help generalize the ultimate solution and, thereby, reduce the total number of calculations that will be necessary to describe the overall behavior.

To quantify the typical orders of magnitude included, the approximate properties and welding parameters for steel are employed. In applications for steel, typical wire diameters are in the range 0.8 to 2 mm (0.03 to 0.09 in.) and wire speeds are of the order 0.04 to 0.2 m/s (100 to 400 in./min). The wire extension beyond the electrical contact tip is about 10 to 30 mm (½ to 1 in.). Typical thermofluid properties of steel (or iron) in solid and liquid phases have been given by Greene (Ref. 8) and Waszink and Piena (Ref. 16) and others.

The Prandtl number of the liquid metal, $Pr = c_p\mu/k$, is a measure of the rate at which viscous effects propagate across the fluid relative to thermal conduction (Ref. 18), or the rate at which the flow field approaches steady state compared to the temperature field. For steel and most liquid metals $Pr \lesssim 0.1$, so the thermal field adjusts to the flow field more quickly than the flow adjusts to its disturbances.

The importance of axial thermal conduction upstream in a fluid (or the solid electrode) relative to the motion can be estimated via the Peclet number,

$$Pe = \frac{Vd}{\alpha} = \frac{\rho V c_p d}{k} = \frac{\rho V d}{\mu}\frac{c_p \mu}{k} = Re \cdot Pr \qquad (2)$$

For $Pe \lesssim 200$, the axial conduction term may be neglected relative to the other terms in the energy equation 1 (Ref. 18). On the other hand, a low Peclet number corresponds to the situation where thermal conduction is much more effective at transporting thermal energy axially than motion of the electrode, as will be seen later.

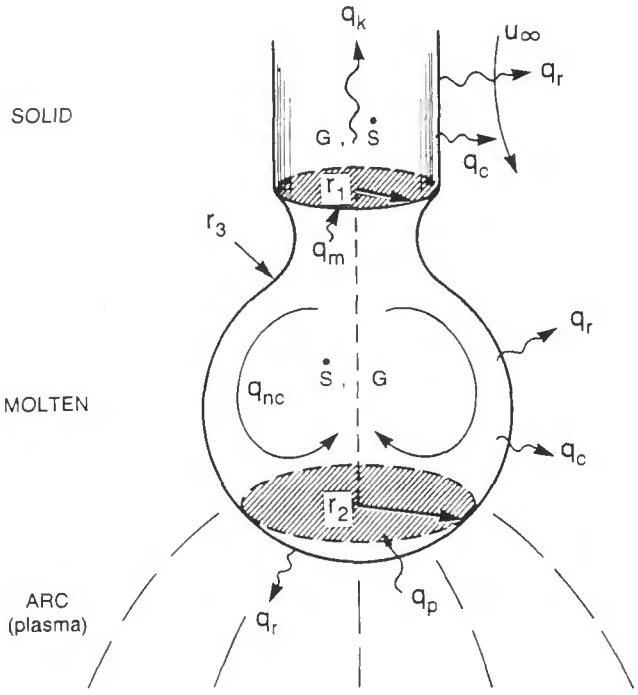

Fig. 1 — Possible thermal processes in an idealized vertical droplet and electrode.

A criterion for the appearance of approximately isothermal conditions is given by the Biot number, $Bi = h \cdot Vol/(k_{solid} \cdot A_s)$, where h is a heat loss coefficient for convection and/or radiation. For the temperature distribution radially across a cylindrical section, it becomes $Bi = h \cdot d/(4k_{solid})$. If $Bi << 1$, the temperature variation across the medium is much less than the difference between the surface and surroundings, *i.e.*, isothermal. Conversely, a large Biot number implies that thermal conduction resistance in the medium dominates the problem establishing the temperature distribution.

Thermocapillary, or "Marangoni," convection has been shown by a number of investigators (Refs. 20, 21) to have significant effects on the thermofluid-mechanics of weld pools. For droplet formation, its effects do not appear to have been considered in detail. Surface tension generally depends on temperature, composition and electrical potential. Lai, Ostrach and Kamotani (Ref. 22) have examined the role of free surface deformation in unsteady thermocapillary flow; while their geometries differ from liquid droplets, their results should provide order-of-magnitude estimates for the present problem. Further, for short times when the motion is still confined to a thin region near the surface, the results for the dissimilar geometries should approach each other, *i.e.*, both cases should be effectively one-dimensional, transient, semi-infinite situations.

The importance of steady thermocapillary convection can be estimated from a number of nondimensional parameters:

1) Static bond number

$$Bd = \frac{\rho g D^2}{\sigma}$$ hydrostatic effects relative to surface curvature effects on pressure

2) Elevation bond number

$$Bo = \frac{\rho g D^2}{|\partial\sigma/\partial T|\,|\Delta T|}$$ $\frac{\text{hydrostatic pressure}}{\text{thermocapillary dynamic pressure}}$

3) Dynamic bond number

$$Bo_d = \frac{\rho g D^2 \beta}{|\partial\sigma/\partial T|}$$ $\frac{\text{natural convection}}{\text{thermocapillary convection}}$

The direction of flow due to thermocapillary convection depends on whether the surface tension increases or decreases with temperature. In a sense, a region with higher σ pulls fluid from regions with lower σ. For very pure steels, $\partial\sigma/\partial T$ is negative so the flow tendency would be from warmer to cooler. In the vertical geometry considered here, that would be from the warm liquid dropping towards the melting zone and thus might inhibit detachment. With small amounts of contaminants, such as sulfur or oxygen, as in the weld pool studies of Heiple and Roper (Ref. 20), $\partial\sigma/\partial T$ can become positive so the tendency would be toward enhancing detachment forces. In either case, the thermal field near the melting interface would be modified to some extent.

To estimate values of the thermocapillary parameters for a liquid steel droplet,

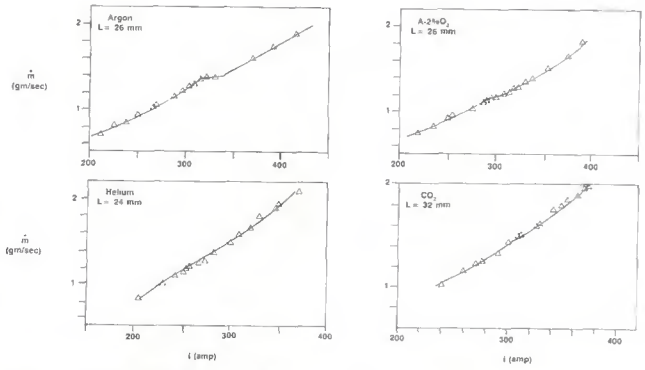

Fig. 2—Melting rate measurements with 1.6-mm steel electrodes.

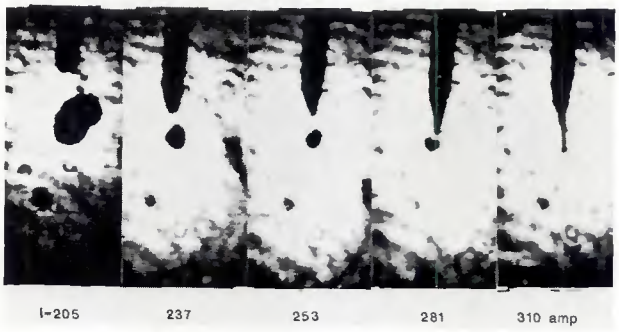

Fig. 4—Effect of electrical current on metal transfer process for steel electrodes with argon shielding.

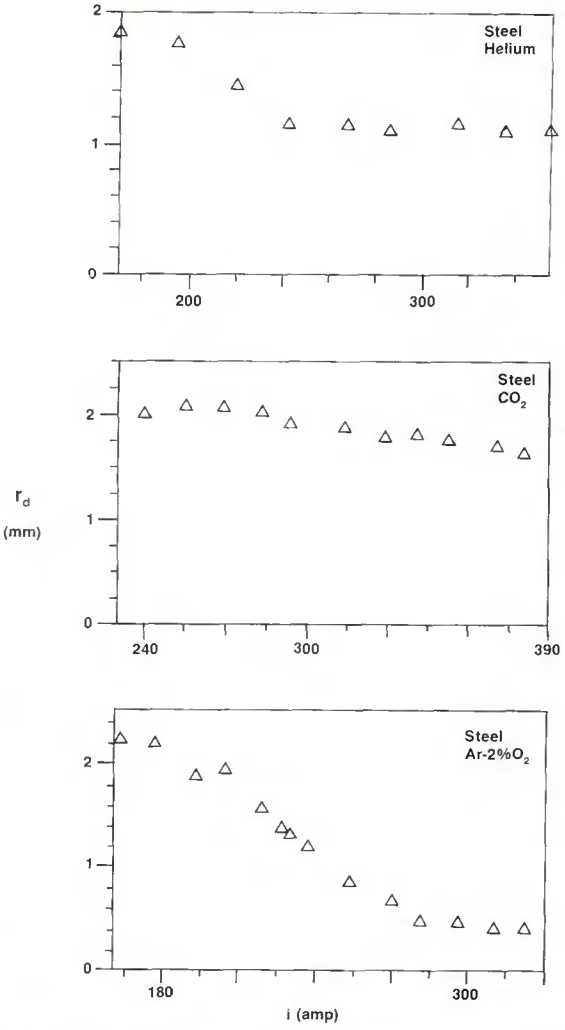

Fig. 3—Effect of shielding gas on droplet size, steel electrodes.

we take the temperature range as being from the melting point to a maximum of about 500 K below the boiling point (Ref. 23). Following Waszink and Graat (Ref. 15), we took surface tension values of $\sigma \simeq 0.9$ N/m (0.005 lbf/in.) and $|\partial\sigma/\partial T| \simeq 0.2 \times 10^{-3}$ N/mK (6×10^{-7} lbf/in. F).

Estimated orders of magnitude and ranges of these thermal parameters are shown in Table 1.

The Biot number refers to radial heat transfer (rather than axial transfer from the liquid droplet to the melting interface). The values of the Peclet number imply that wire motion is more significant but that axial thermal conduction is not entirely negligible.

With the exception of Bo for globular transfer and Bo_d for spray transfer, the thermocapillary parameters are all of order one, which illustrates the complexity of determining heat transfer behavior within the liquid droplet. The value of the static Bond number (Bd) near unity for globular transfer is an indication why simple gravitational force balance analyses give reasonable predictions for this mode of metal transfer. For globular transfer, hydrostatic pressure would be expected to be significantly greater than the thermocapillary dynamic pressure since $Bo >> 1$. And for spray-sized droplets, Marangoni convection would be significantly greater than natural convection ($Bo_d << 1$). The value of $Bd \simeq 0.2$ for spray transfer would be an indication that a force(s) other than gravity (such as electromagnetic forces and/or so-called plasma jet drag) is involved in droplet detachment in that mode, since surface curvature would cause greater pressure (and restoring force) than the weight of the drop. Greene (Ref. 8) and Waszink and Piena (Ref. 16) have concluded from different arguments that the additional forces are electromagnetic and, therefore, Maxwell's equations should be included in the complete solution. While plasma jet drag can be expected to be significant as the free droplet passes through the arc region, it is not clear that it would have an important effect while the droplet is still attached. It is anticipated that it would primarily act indirectly through its upstream influence on the shielding gas around the drop, partially countering the deceleration of the gas at the bottom of the drop (*i.e.*, pressure recovery and negative drag). Treatment of this aspect would require a more complete analysis, including the plasma arc, that is beyond the scope of this paper.

The discussion of the nondimensional governing parameters above applies primarily to steady processes. However, droplet formation and detachment is a nonsteady event, so time scales or response times of the phenomena must also be considered to estimate whether steady or quasi-steady conditions may be approached during the process (Ref. 24).

For 1.6-mm (1/16-in.) diameter mild steel, Lesnewich (Ref. 3) shows droplet detachment frequencies to be of the order of 15/s for currents below 240 A and 250–300/s above 280 A. These values represent globular and spray metal transfer and correspond to periods of about 70 ms and 3 ms, respectively. Kim (Ref. 19) observed frequencies ranging from about 3 to 450/

Table 1—Estimated Orders of Magnitude

	Pe	Bi	Bd	Bo	Bo_d
Globular	4	0.001	2	10	0.8
Spray	40	0.001	0.2	1	0.08

s. For his experiments with 1.1-mm (0.045-in.) diameter steel, Morris (Ref. 25) reports typical values of 50 ms for globular and 4 ms for spray transfer but has seen up to 2000 drops/s or droplet periods as short as ½ ms.

The time for a thermal change to approach steady state (within about 5%) by conduction in the radial direction (Ref. 26), the thermal conductive time scale, can be estimated as $\Theta_T \simeq 0.6\, r_o^2/\alpha$.

The viscous time scale to approach steady state can be expected to be analogous to the thermal conductive time scale, or $\Theta_V \simeq 0.6\, r_o^2/\nu = 0.6\, \Theta_T/Pr$. (Allum (Ref. 12) quotes Sozou and Pickering (Ref. 27) as saying that for J × B flows to approach steady state requires $\Theta \sim L^2/\nu$, *i.e.*, another viscous time scale.) Temperature variation near the surface affects the surface tension and, therefore, the droplet shape particularly near the neck at detachment. Consequently, one must consider the time necessary to modify the surface layers rather than only the approach to steady state. For radial conduction in a cylinder, a 90% change in temperature is predicted at $r/r_o = 0.9$ within nondimensional time $(\alpha\Theta/r_o^2) \simeq 0.1$, approximately. This time scale is about ⅙ of that for full thermal penetration (*i.e.*, response "penetrates" from surface to centerline) and we refer to it as response of the surface layer.

For their weld pool simulation Kou and Wang (Ref. 28) claim the characteristic time associated with electrical conduction are of the order of 10^{-12} s. Since these time scales probably have an r^2 dependence and the weld pool covers a larger region than the droplet, the corresponding times can be expected to be negligible in the present problem. Typically, power supplies show a ripple of about 5% or more in the electric current (unless they are stabilized) at 60, 120 or 360 Hz. This situation implies about a 10% variation in i^2 with a period of 16, 8 or 3 ms, respectively. Thus, this process is usually slow relative to spray detachment but is fast relative to globular detachment. Nonetheless, in either case it could be expected to influence the detachment process upon which it is superposed.

A time scale for the propagation of capillary waves can be formed from the fluid properties as $\Theta_c = [8\sigma/(\rho g^3)]^{1/4}$. For steel it is of the order 30 ms, which is slow compared to the period for spray transfer and the same order or faster than the period for globular transfer. These relative

Table 2—Orders of Magnitude of Electrode Time Scales[a]

	Globular	Spray
	(Values in milliseconds)	
Droplet period	50–70	2–3
Electrical conduction	$<10^{-9}$	$<10^{-9}$
Current oscillations (60, 120, 360 Hz)	16, 8, 3	16, 8, 3
Shielding gas residence time	4	1
Viscous diffusion to center	2500	40
Thermal conduction to center	300	20
Thermal surface layer ($r \gtrsim 0.9r_d$)	50	3
Capillary waves	30	30
Surface oscillation	16	2
Thermocapillary (Marangoni)[b]		
a) Significant surface velocity increase	60	4
b) Surface velocity approaches electrode feed velocity	4	0.3
c) Surface fluid particle travels $\pi d_d/2$ due to T/dx, steady state	2	0.4
d) Surface fluid particle travels $\pi d_d/2$ in flow induced during typical droplet period	60	20

(a) Steel, 1.6 mm (1/16 in.) diameter.
(b) See text for further explanation.

Fig. 5—Current path indications with argon shielding.

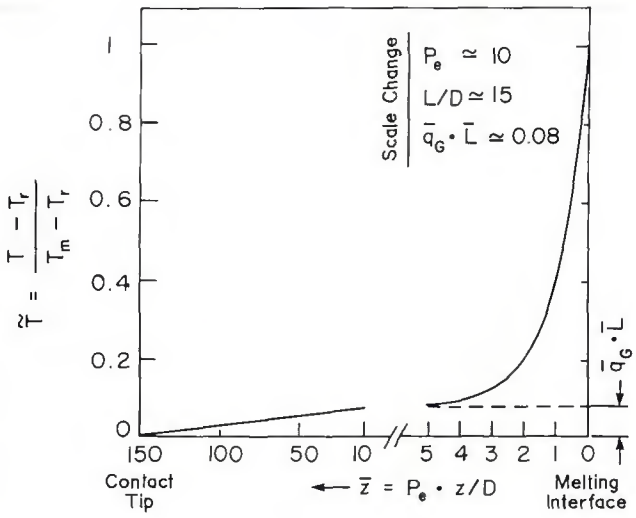

Fig. 6 – Approximate axial temperature variation for steel electrodes as predicted by one-dimensional analysis based on constant properties, $i \simeq 200^+$ A.

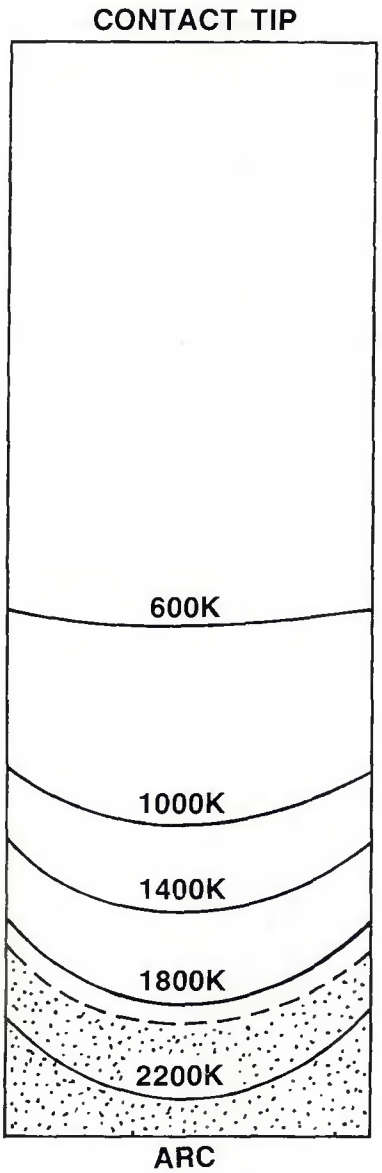

Fig. 7 – Typical temperature distribution in the electrode as predicted by the PHOENICS code, $\alpha = 0.3$, $i = 280$ A.

times explain why surface waves are observed in the globular mode but few such waves are seen in spray transfer. The natural frequency of the fundamental mode for surface oscillation of a sphere of liquid surrounded by an infinite region of gas (Refs. 29, 30) can be approximated as $f^2 = 16\sigma/(\pi^2 \rho d^3)$. A time scale to correspond to a significant surface oscillation might be taken as about one-eighth of the period during the cycle of oscillation.

Lacking a transient solution for thermocapillary flow in a suitable axisymmetric geometry, we developed several approximate estimates in an effort to deduce orders-of-magnitude for thermocapillary time scales. The four approximations were:

1) Time for significant velocity increase after imposing a temperature difference on a thin liquid layer (Ref. 31), $\Theta \simeq 0.1\Theta_M \simeq 0.1\, h^2/\nu$.

2) Time from imposition of temperature difference on thin liquid layer until induced surface velocity becomes comparable to electrode feed velocity.

3) Residence time for surface particle (time to traverse half circumference) at steady conditions based on axial temperature gradient.

4) Residence time corresponding to flow induced during a typical droplet period, starting from rest (Ref. 22) – Fig. 4. Estimates are included in Table 2. Further details are in the report by McEligot and Uhlman (Ref. 24). These four different approaches give a range greater than an order of magnitude for the possible thermocapillary time scales.

The results of the time scale estimation for 1.6-mm (1/16-in.) diameter steel are presented in Table 2. It must be emphasized that these are merely order-of-magnitude estimates for guidance. In general, when the response for one phenomenon is much quicker than another, the first can be treated as quasi-steady relative to the second. When time scales are of the same order, both phenomena must be considered in the transient analysis. From the comparison, we see that viscous diffusion is too slow to be important except as involved in the thermocapillary surface phenomena. The proper time scale for thermocapillary convection in this application has not been determined. Due to the range of values estimated, one can only say it may be important for globular and/or spray transfer. For globular and spray modes, thermal conduction at the surface and surface oscillations have time scales comparable to their periods. Interaction with electric current oscillations depends on the power supply frequency (and whether it is stabilized effectively).

In summary, for the general case of electrode melting and detachment, the order-of-magnitude estimates of governing parameters and time scales reveal no significant simplification except that buoyancy forces are likely to be negligible in the droplet. Further, since a number of time scales are of the same order-of-magnitude, the fluid and heat transfer problems in the liquid droplet should not be considered to be quasi-steady processes. A steady-state analysis (which might be attempted with some available codes) would be inappropriate and perhaps misleading. Ultimately, it will probably be necessary to solve the transient, coupled thermofluidmechanic equations for the droplet and wire in conjunction with experimental observations to obtain predictions with reasonable detail. The present study begins that process, concentrating on the solid electrode.

Melting Experiments

Measurements were obtained with research welding equipment to observe the electrode shape, arc attachment, droplet size, transfer modes and their relationships to typical welding control parameters. These experiments established the conditions for which numerical simulations were later conducted.

Apparatus

Direct current electrode-positive (DCEP) welding was performed in the constant current mode using an electrode feed motor, which was regulated by the arc voltage signal. Current was controlled by a 20 kW analog transistor power supply designed by Kusko (Ref. 31), which supplied current with less than 1% ripple. In order to control variations in resistive heating of the electrode extension, an alumina tube was inserted into the contact tip, leaving only 5 mm (0.2 in.) for electrical contact rather than the customary contact length variation of 24 mm (1 in.) in this commercial electrode holder (Ref. 19).

Analysis of the metal transfer process was performed using high-speed video-

photography at 1000 fps. In contrast to the conventional high-speed cinematography, which uses a light source with greater intensity than the arc and a strong neutral-density filter, a laser backlit shadowgraphic method (Ref. 33) was used in this study. This system excludes most of the intense arc light and transmits most of the laser light by placing a spatial filter at the focal point of the objective lens. The system setup and the equipment specifications are detailed by Kim (Ref. 19).

Procedures and Ranges of Variables

Measurements emphasized mild steel (AWS ER70S-3) as the electrode material but aluminum alloys (AA1100 and AA5356) and titanium alloy (Ti-6Al-4V) were also employed to include a wider range of physical properties. An electrode diameter of 1/16 in. (1.6 mm) was used throughout. The shielding gases used were pure argon, pure helium, their mixtures, argon-2% oxygen and carbon dioxide. The ranges of variation of welding parameters during this study are given in Table 3. Overall welding current ranged from 80 to 420 A and electrode extension was set at 16, 26 or 36 mm (0.63, 1.02 or 1.4 in.).

Electrode extension is defined in this study as the distance from the end of the contact tip to the liquid-solid interface. With the video monitoring technique, it could be controlled within ± 1 mm (0.04 in.) during welding. Electrical current was measured by an external shunt, which is capable of measurement within an uncertainty of ± 1% of full scale.

Melting rates were measured by reading the output voltage of a tachometer, which was in contact with the moving electrode. The tachometer was carefully calibrated by indenting the surface of the electrode once every second with a solenoid indenter triggered by a rotating cam. Afterwards, the indented sections of the electrode were removed and the actual mass of the electrode passing through the system per unit time was measured to an accuracy of 0.0005 g. In addition, the calibration was performed by measuring the mass that passed through the indentor for 5 s.

Experimental Results

Typical data for melting rates (or wire feed speeds V_w) with steel and a range of shielding gases are presented in Fig. 2. The same trends were seen at shorter and longer extensions (Ref. 19). With argon, as well as with A-2%O_2, there is an apparent slight variation in the trend of the curve, or a transition at intermediate currents. With helium and carbon dioxide as shielding gases, this effect was not evident; the slopes of the curves were continuous and nearly constant.

For mixtures with an argon-rich composition (75% A/25% He) there also is an apparent transition in the melting rate curve. However, as the helium content is increased (50% A/50% He), the transition disappears. Aluminum and titanium revealed slight transitions in their curves when shielded with pure argon. Thus, it seems that the transition is related to arc behavior with argon shielding gas.

For the same variety of welding conditions, droplet sizes were determined. The size was measured from the still image on the video screen once every 10 s, then these ten samples were averaged. Figure 3 compares the results for steel with A-2%O_2, helium and CO_2 as the shielding gases. Again there is a substantial difference in behavior depending on shielding gas, but no critical transition in size is observed. Calculations of the related droplet detachment frequencies also failed to show any sharp transition. However, with argon, much smaller droplets are evident at high currents.

Visualization of the electrode and droplet detachment provides some insight into the effects of argon on the metal transfer process. Figure 4 demonstrates the effect of electrical current on the size of the detached droplets and the shape of the solid electrode for steel and argon over the same range as Figs. 2 and 3. A continuous, gradual variation is seen. If one defines the transition to spray transfer as occurring when the droplet diameter is approximately equal to the wire diameter, it is seen in the middle sub-figure for $i \simeq 253$ A. This value agrees with the observations of Figs. 3. This gradual transition contradicts work in the 1950s, which reported a sharp transition (Refs. 2, 3), but is consistent with all follow-on studies performed over the past 30 years.

At low currents, the photographs show large subglobular droplets and a relatively blunt tip to the electrode. As the current is increased: 1) the droplets become smaller, 2) the required wire speed increases and 3) the electrode tip acquires a sharpening taper. The sequence is continuous and gradual.

No taper was observed with shielding by helium or CO_2, but visualization showed a repelled form of detachment, which led to large drop sizes. With aluminum and argon shielding, a taper formed

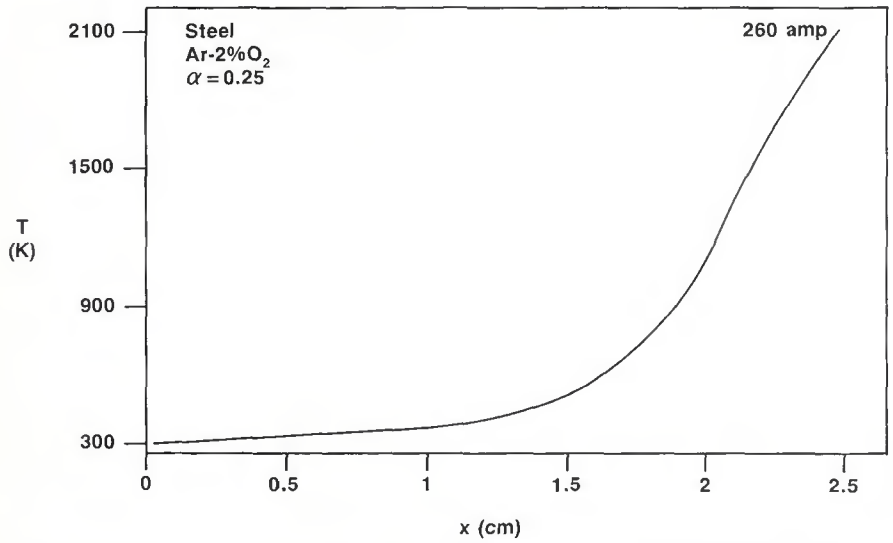

Fig. 8 – Axial temperature distribution along electrode centerline as predicted by the PHOENICS code.

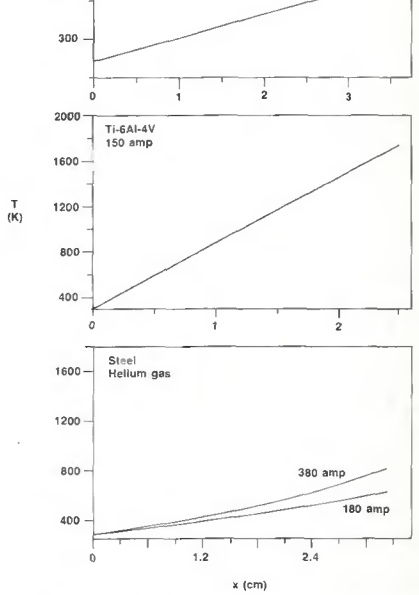

Fig. 9 – Predicted axial temperature distribution with negligible electron condensation on side surface ($\alpha \simeq 0$).

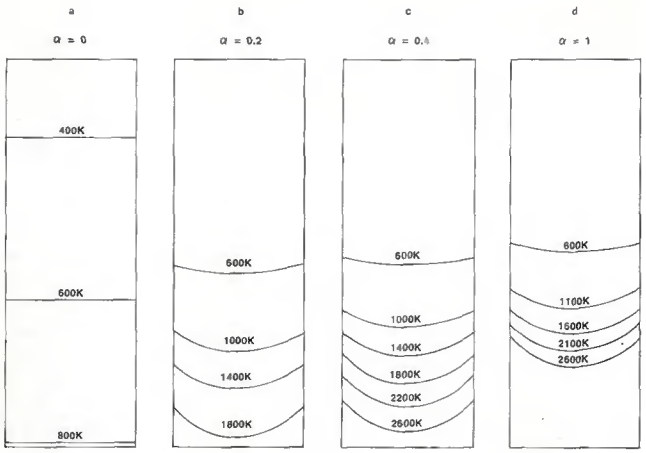

Fig. 10 – Predicted effect of electron condensation on side surface of solid electrode.

but was shorter (or blunter) than for steel. None was seen for DC operation of titanium electrodes to 260 A (maximum used), but it did occur with pulsed currents at 500 A, so it is expected for higher DC currents with argon.

Consideration of the electron current path yields further understanding. The distribution of current on the surface of the electrode is affected by several factors, such as material, shielding gas and total welding current. Precise measurement of the distribution is not available. However, in Kim's study (Ref. 19), an approximate method, considering the main current path to be related to the bright spots on the photographs, gave useful indications. These observations of anode spot behavior were made with a color video camera using the laser backlight system. Instead of the narrow band filter used with the high-speed video, a neutral-density filter was used to adjust the light input to the camera.

Figure 5 shows observed bright spots or indicated current paths for steel and titanium alloys in globular transfer and steel in streaming transfer, all with argon. In steel, there is no well-defined current path into the consumable electrode. Rather, the arc root appears to be diffuse. Therefore, it seems that the electrons condense not only on the liquid drop, but also on the solid side surface of the electrode. Comparable phenomena were observed with aluminum. With the titanium alloy there is a sharp anode spot on the liquid drop, with a strong plasma jet emanating from this spot, and most of the electrons seem to condense on the liquid drop at this spot.

With CO_2 shielding, most of the electrons condense at the bottom of the liquid drop. With helium, the electron condensation is confined to the lower bottom but is less concentrated than with CO_2 (Ref. 19).

As a consequence of the above observations, the following hypotheses of taper formation is proposed (Ref. 19): When the shielding gas is argon, a portion of the electrons condense on the cylindrical side surface of the solid electrode and liberate heat of condensation at this location. When this energy generation rate is high enough on the surface, the electrode surface will melt and the liquid metal film will be swept downward by gravitational and/or other forces. When this melting occurs over a sufficient length of the cylinder, a taper will develop at the end of the electrode. Whether this hypothesis is quantitatively consistent with the thermal phenomena in the solid electrode is a question that is examined analytically in the later sections.

Preliminary Analyses for Solid Electrode

As an introduction to the next section, and to provide further insight, this section provides discussion of a limiting closed form analysis. By treating the material properties as constant and the electrical and thermal fields as steady, one may approximate the thermal behavior in the solid electrode by two limiting cases: 1) resistive heating without heat transfer through the side surface (*i.e.*, one-dimensional), and 2) heating at the side surface without axial conduction. The first corresponds to the observations where no significant current path to the side of the electrode was apparent, and the second represents the situation hypothesized above as leading to taper formation. Closed form analyses are possible for both cases.

The steady idealization implies that the dimensions of interest are large relative to the penetration depth (*i.e.*, depth to which the thermal oscillation is significant) for thermal conduction at the droplet detachment frequencies and/or that the predictions represent effective temporal averages. This penetration depth can be estimated from the transient conduction solution for a cosinusoidally oscillating surface temperature on a semi-infinite solid (Ref. 34, Equation 6.12a). For the n-th harmonic about the mean it takes the form

$$T-T_{mean} = T_o \exp\left\{-\left(\frac{n\pi}{\alpha P}\right)^{1/2} x\right\}\cos\left\{\frac{2\pi n}{p}t-\left(\frac{n\pi}{\alpha P}\right)^{1/2} x\right\} \quad (3)$$

The depth at which the amplitude is a fraction $1/v$ of the surface amplitude is then

$$\Delta x = (\ell n\, v)\cdot\sqrt{\alpha P/(n\pi)} \quad (4)$$

From the first harmonic and a 5% criterion, one may estimate this penetration depth to be about $0.1d_w$ for spray transfer and $0.6d_w$ for globular transfer for steel in the present experiments. There may be a bit more variation due to the actual size of the drops, but it would be countered by the convective wire motion in the opposite direction to the thermal disturbance.

The treatment of heating of the side surfaces by electron condensation involves the solution of Equation 1 as a partial differential equation. With suitable idealizations the problem may be attacked with superposition techniques employed for convection heat transfer in the entrance of a heated tube (Ref. 18) or transient conduction in a rod (Ref. 34). Application of such an analysis to the moving electrode problem is under development by Uhlman (Ref. 35), but it is considered beyond the scope of the present paper. Thus, we will concentrate on the first (one-dimensional) situation for preliminary, closed form analysis.

The one-dimensional idealization corresponds to conditions where all heating by electron condensation occurs at the tip, and there is no significant heat loss (or gain) at the cylindrical surface of the electrode. In this situation, the governing energy Equation 1 may be reduced and nondimensionalized to an ordinary differential equation.

$$\frac{d^2\bar{T}}{d\bar{z}^2}+\frac{d\bar{T}}{d\bar{z}} = \bar{q}_G \quad (5)$$

where $z = L - x$ is measured from the molten tip so $u = -V_w$ and the nondimensional variables are

$$\bar{T} = (T_m - T)/(T_m - T_r)$$

$$\bar{z} = (V_w z/\alpha) = zPe/D$$

and

$$\bar{q}_G = \frac{q_G''' D^2}{k(T_m - T_r)Pe^2} = \frac{16}{\pi^2}\frac{i^2\rho_e}{kD^2(T_m - T_r)Pe^2} \quad (6)$$

Appropriate boundary conditions are

$$\bar{T} = O \text{ at } \bar{z} = O$$

$$\bar{T} = 1 \text{ at } \bar{z} = \bar{L} = LPe/D \quad (7)$$

The solution of this mathematical problem with $\bar{q}_G$ taken constant may be written

$$\bar{T}(\bar{z}) = (1 - \bar{q}_G\bar{L})\left[\frac{1 - e^{-\bar{z}}}{1 - e^{-\bar{L}}}\right] + \bar{q}_G \cdot \bar{z} \qquad (8)$$

where the first term represents the contribution of the thermal conduction from the molten interface, transported upstream against the motion, and the second is the consequence of resistive heating by the electrical current. In a previous section, we saw that for steel electrodes we can expect $4 \lesssim Pe \lesssim 40$ and in the experiments L/D was about 10 to 20 so the denominator is near unity, giving the approximation

$$\bar{T}(\bar{z}) \simeq (1 - \bar{q}_G\bar{L})\ [1 - \exp{-\bar{z}}] + \bar{q}_G\bar{z}$$

or

$$\tilde{T} = \frac{T - T_r}{T_m - T_r} \simeq 1 - \bar{q}_G\bar{z} - (1 - \bar{q}_G\bar{L})\ [1 - e^{-\bar{z}}] \qquad (9)$$

which is unity at the molten tip and decreases to zero approaching the contact tip at $\bar{z} = \bar{L}$.

Equation 9 is presented for typical conditions in Fig. 6. The parameters employed in this calculation are L/D = 15, Pe = 10 and $\bar{q}_G$ corresponding to slightly more than 200 A in a 1.6-mm (1/16-in.) diameter steel electrode with electrical resistivity evaluated at an intermediate temperature of about 800°C. The exponential term in Equation 8 or 9 (or the right-hand side of Fig 6) shows that the effect of thermal conduction from the melting interface becomes negligible beyond $\bar{z} \gtrsim 5$ or $z/\tilde{D} > 5/Pe$. For even the lowest Peclet number expected, this is only of the order of one diameter upstream. As V (and therefore Pe) increases, the distance becomes less yet.

The fraction of the total temperature rise from T_r to T_m due to conduction from the interface is approximated by the term $(1 - \bar{q}_G\bar{L})$. The nondimensional quantity q_G may be seen to be the asymptotic slope of the curve $\bar{T}(\bar{z})$ away from the molten tip. For $i \simeq 200$ A at 1000 K with 1.6-mm steel, typical values would be of the order $\bar{q}_G \simeq 0.5/Pe^2$. However, it must be reemphasized that these results can only be considered qualitative. The quantity $q_G(\bar{x})$ varies substantially since ρ_e increases by a factor of about eight for steel between T_r and T_m so the slope of the contribution by resistive heating will also increase as T_m is approached.

Effects of choice of other materials may be estimated via Equation 9. For example, for aluminum at the same electrode velocity as steel, Pe will be less by a factor of about six, so conduction upstream from the molten interface would be significant about six times further. For the same electrical current, $\bar{q}_G$ decreases both due to the increase in thermal conductivity and the decrease in electrical resistivity. Therefore, $\bar{q}_G\bar{L}$ is expected to be considerably smaller for aluminum than steel and much less melting would be due to resistive heating.

Numerical Predictions for Solid Electrode

The purpose of the numerical analyses is to provide means of examining whether the hypothesis of arc heating of the sides of the electrode is consistent with the thermal observations of the experiments. Thus, calculations were conducted at conditions corresponding to some of the individual experiments.

The thermal problem was approximated as steady, with time-averaged values from the experiments used for boundary conditions where necessary. For steady motion of the solid electrode, the governing thermal energy Equation 1 may be reduced and rearranged to

$$\rho V_w \frac{\partial H}{\partial x} = \frac{\partial}{\partial x}\left(\frac{k}{c_p}\frac{\partial H}{\partial x}\right) + \frac{1}{r}\frac{\partial}{\partial r}\left(\frac{kr}{c_p}\frac{\partial H}{\partial r}\right) + q_G''' \qquad (10)$$

The resistive heating term can be evaluated as

$$q_G''' = J^2\rho = i^2 p/(\pi r^2)^2 \qquad (11)$$

provided the electrical current density is taken as uniform across the cross-section. Preliminary numerical solutions of the (electrical) potential equation demonstrated this assumption to be valid for the purposes of the present work.

The temperature dependencies of the steel properties may be expressed as piecewise-continuous polynomials over successive temperature ranges. For example, electrical resistivity may be represented as

$$\rho_e(T) = a_1 + b_1T + c_1T^2 \quad \text{for } T < T_1 \qquad (12)$$

$$= a_2 + b_2T + c_2T^2 \qquad \text{for } T_1 < T < T_2$$

and so forth.

Appropriate steady thermal boundary conditions are:

Uniform inlet temperature, $T = T_r$ at $x = 0$ (13)

Gaussian surface heat flux due to electron condensation,

$$q_s'' = \frac{\alpha i v_c}{\pi r_w} \cdot \frac{1}{\sigma\sqrt{2\pi}} \exp\left\{-\frac{(L - x)^2}{2\sigma^2}\right\} \text{ at } r = r_w \qquad (14)$$

where $V_c = (3kT/2e) + V_a + \phi$. Uniform interface heat flux at electrode tip,

$$q_i'' = (q_{total} - q_s - q_G)/\pi r_w^2 \quad \text{at } x = L \qquad (15)$$

Radiation and convection losses from the heated electrode can be accounted for with q_s or may be neglected. A measure of the length of the wire surface heated by electron condensation is given by the Gaussian distribution parameter, σ, and α is the fraction that occurs on the side surface. The quantities V_a and ϕ represent anode voltage drop and work function, respectively. The total energy transfer rate q_{total} is given by

$$q_{total} = \dot{m}\Delta H + \rho V_w \pi r_w^2 \Delta H \qquad (16)$$

where ΔH is the enthalpy increase above the reference temperature required to melt a unit mass of the material.

When there is electron condensation on the wire surface, the electric current varies along the electrode, so the resistive heating term would not be constant even if the electrical resistivity were independent of temperature. The assumed Gaussian distribution for electron condensation requires the electrical current density to vary axially as

$$J(x) = \frac{\alpha i}{\sqrt{2\pi^3 r_w \sigma}} \exp\left\{-\frac{(L - x)^2}{2\sigma^2}\right\} \qquad (17)$$

This relation must be applied with $\rho e(T)$ in evaluating q_G'''.

If the material properties could be approximated as constant with temperature, the energy equation would become linear and, conceptually, might be solved analytically in closed form. As noted by Kays (Ref. 18), if the Peclet number is sufficiently high, the axial conduction term can be neglected and the problem would reduce to a convective thermal entry situation (*i.e.*, growth of thermal boundary layers from the surface into the moving medium as in the entry of a heated tube). The solid electrode motion corresponds to a "plug flow" for which classical solutions are available (Stein, 1966), and an approximation of the surface boundary condition can be introduced by superposition techniques (Ref. 35).

Since the material properties do vary substantially with temperature, particularly across the fusion zone, an iterative numerical technique was applied via an axisymmetric version of the so-called PHOENICS code. This code is a general thermofluidmechanics computer program developed by CHAM, Ltd., from the earlier work of Patankar and Spalding (Refs. 36, 37) to solve coupled sets of partial differential equations governing heat, mass and momentum transfer (Ref. 38). For the present work, an axisymmetric version was applied to solve the thermal energy Equation 10 alone, employing the boundary conditions and thermal properties described above. The velocity was taken as uniform at V_w throughout the field, so it was not necessary to solve the momentum equations.

Some aspects of the melting phenomena were simulated by employing the enthalpy method (Refs. 39, 40). Enthalpy is taken as the dependent variable as in

Equation 10 and conversion to temperature via the property relation T(H) can account for the heat of fusion and phase transformation (*e.g.*, γ to α) in addition to the varying specific heat of the solid. However, the velocity and boundaries of the solution region were kept fixed so convection and free surface phenomena in the molten liquid were not treated. Further, since the main interest in the present study focused on the solid region, most of the simulations neglected the treatment of melting and phase transformation. The effect of phase transformation was tested with comparative calculations and was found negligible.

Calculations were essentially simulations of individual melting experiments. Electrode diameter was taken as 1/16 in (1.6 mm) and properties were for the material used, usually steel. The electrode extension L, electrode feed speed V_w and electrical current i were as measured in the specific experiment. The quantities q_{total} and q_s were estimated from the experimental measurements via Equations 16 and 14, respectively. The resistive energy generation rate q_G was evaluated via integration and Equations 11, 12 and 17 during the iterative solution.

A fixed numerical grid was employed. Twenty nodes were distributed uniformly in the radial direction between the centerline and the surface and 80 in the axial direction, also equidistant. The solutions were obtained via a transient approach to steady state. At each step, the enthalpy distribution was determined via the energy equation and the local temperatures and other properties were then determined from the property relationships. Iterations continued until they converged within 0.001% of the temperature at successive time steps.

Inlet temperature at the contact tip was taken as the measured room temperature, about 300 K. An approximate calculation by Kim (Ref. 19) demonstrated that the convective and radiative heat losses from the electrode would be less than one per cent of the energy rate required for melting. In other preliminary calculations, numerical solutions with surface heating q_s set to zero were compared to the one-dimensional analytic solution that applies if properties are constant. The axial temperature distribution predicted numerically with allowance for property variation, agreed reasonably.

The effect of shielding gas was introduced via the parameter α, which is the fraction of energy received via electron condensation on the electrode side surface relative to the total electron condensation. Based on the experimental observations of the arc and electrode, the values shown in Table 4 were chosen. (Practical thermal field solutions presented later suggest α varies from 0.1 to 0.25 for steel with argon.) Variation of the Gaussian distribution parameter was examined (Ref. 19), but a value σ = 0.35 cm (0.14 in.) was employed unless stipulated otherwise. This value was based on estimates of the radial distribution of current density in a welding plasma (Ref. 41).

In the regions where predicted temperatures exceeded the melting temperature, the velocity was still taken as the wire feed speed V_w. Thus, possible relative motion of the molten liquid was neglected and no liquid film flow was simulated along the tapering interface observed in some experiments.

Typical predictions are demonstrated in Fig. 7. Steel is simulated with argon shielding, electrode extension of 2.6 cm (1.02 in.), wire feed speed of 6.6 cm/s (2.6 in./s) and electrical current of 280 A. The nondimensional velocity is Pe $\simeq$ 14. The value α = 0.3 is used for the electron condensation parameter in this case. Selected isotherms are plotted across a vertical centerplane of the electrode via an assumption of symmetry. Motion is vertically downward as in the experiment. The crosshatching represents the region where the temperature is predicted to exceed the melting temperature.

It is evident that outer surface heating and thermal conduction in the solid initiated the growth of a thermal boundary layer from the surface above the 600 K isotherm. As a consequence of the increased temperature near the surface, the electrical resistivity (and therefore q_G''') is increased there, raising the temperature further. This thermal boundary appears to have penetrated almost to the centerline by the second isotherm at 1000 K. For comparable laminar flow in tubes, fully established Nusselt numbers are expected to require a nondimensional distance $L^+ = (x/r_w)/Pe = 0.1$ or so without axial conduction (Ref. 18). For the conditions of this simulation that criterion corresponds to 0.7 diameters, but the distance for the temperature profile to become approximately invariant would be longer.

Below the melting isotherm (~1900 K), the steel is predicted to be molten. In practice, the liquid motion would depend on gravity and electromagnetic forces (accelerating forces) in relation to the electrode feed speed (momentum). At low V_w, one would expect a liquid film to form at the surface when $T(x,r_w) = T_m$ and to run down the solid surface, forming a taper and droplet as in the spray transfer experiments. At high V_w (therefore, high current) there may be insufficient time for the liquid film to clear so the molten region may continue to move in "solid body motion" as some cases of streaming transfer appear. The present simulation does not discriminate between these two cases. Instead, it represents a form of average cylindrical equivalent to the solid-plus-liquid regions of the electrode with their interface falling in the interior.

Figure 8 presents the axial temperature profile along the electrode centerline for approximately the same situation (here α = 0.25 and i = 260 A). During the first half of the travel, the temperature increases slowly due to electrical resistance heating, and there is a slight increase in slope as ρ_e increases with temperature. Near x $\simeq$ 1.4 cm, the hypothesized surface heating begins to affect the centerline temperature. This observation corresponds to the propagation of the apparent thermal boundary layer as described above. As T approaches T_{melt}, there is also a further increase due to thermal conduction upstream from the melting interface, in accordance with Equation 8 or 9 evaluated near x = L (*i.e.*, near z = 0). The upstream propagation could be estimated to be the order of $x/r_w \simeq 10/Pe$ or 0.6 mm. The near-linear increase of T(x) toward the end of the electrode is likely to be a fortuitous consequence of countering effects of thermal boundary layer growth, the Gaussian increase of q''_s with x and upstream conduction.

Table 3—The Combination of Welding Parameters Used in Experiments

	Shielding Gas			Electrode Extension	Arc Length	Welding Current
	Argon	Helium	CO_2	(mm)	(mm)	(amp)
Mild steel	x[a]	x	x	16,26,36	14 – Ar 6 – He 8 – CO_2	180–420
Aluminium (1100, 5356)	x			16,26,36	14 – Ar	80–220
Ti-6Al-4V	x		x	16,26,36	14 – Ar	120–260

(a) Welding was performed.

Discussion of Results

As noted earlier, the temperature distribution in the solid electrode is primarily affected by the resistive heating, heat transfer via the liquid drop and electron

Table 4—Values Assigned According to Experimental Observations

Electrode	Gas	α
Steel	Helium, CO_2	θ
Steel	Argon-2%O_2	Varied $0 \rightarrow 1$
Titanium (Ti-6Al-4V)	Argon	0
Aluminum	Argon	0

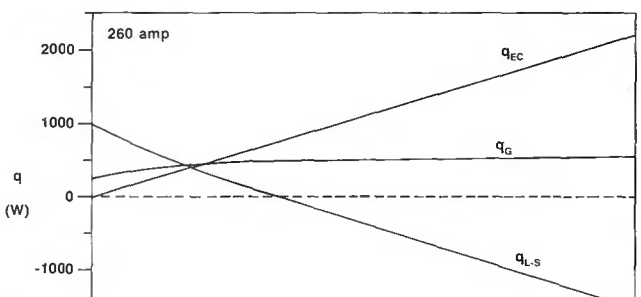

Fig. 11—Predicted effects of electron condensation ratio α on thermal energy balance for steel electrodes with argon shielding.

condensation on the cylindrical side of the electrode. Measurement of these quantities is impractical, if not impossible, so indirect methods become necessary to evaluate them. In this section, the numerical technique previously discussed is applied to deduce quantitatively whether electron condensation is a reasonable explanation for the tapering of steel electrodes in argon shielding, to estimate its rate and, then, to determine the relative magnitudes of these thermal phenomena. Electron condensation on the side surface is represented by α, the ratio at the side to the total condensation on the liquid droplet plus side. In a sense, the numerical solution is used to calibrate α for the conditions of the experiments.

Effects of Side Electron Condensation on Temperature Distribution

Examination of the visual observations led to the conclusion that there was no significant electron condensation on the electrode side for aluminum or titanium alloys or for steel shielded by helium or carbon dioxide. Therefore, in these cases, $\alpha \simeq 0$. The problem becomes one-dimensional in space with uniform temperatures in the radial direction. The axial temperature distribution could be predicted by Equation 8 if the properties did not vary significantly with temperature. To account for the property variation, the numerical solution was obtained.

Figure 9 presents the predicted results at typical experimental conditions for these materials and shielding gases with $\alpha = 0$. A typical two-dimensional prediction for this case is included as Fig. 10A, demonstrating the one-dimensional isotherms or uniform radial temperature profiles. For aluminum, the low electrical resistivity yields very little resistive heating and only a slight temperature increase along the electrode. Thus, the increase to the melting point must be provided almost entirely by thermal conduction from the melting interface, comparable to the bracketed term in Equation 8. On the other hand, the electrical resistivity of the titanium alloy is high so most of the approach to melting is due to resistive heating—Fig. 9B.

For steel electrodes, the thermal variation of electrical resistivity is more significant, as demonstrated by the nonlinear temperature variation in Fig. 9C with helium shielding. With carbon dioxide shielding, comparable results are predicted, but the temperature is a bit higher at a given current because the electrode velocity (melting rate) is less. An effect of electron condensation on the cylindrical side can be seen by comparison to Fig. 8, which is for $\alpha = 0.25$, simulating argon shielding. In the latter case, the induced temperature rise is substantial and approaches the melting temperature near the end of the electrode.

The predicted effect of α on the internal temperature of the electrode is demonstrated in Fig. 10 with variation from zero to unity (*i.e.*, no electron condensation on the side to all on the side surface). These simulations represent steel with argon shielding with an electrical current of 280 A. The length shown corresponds to the measured extension length. With $\alpha > 0$, the temperature profile shapes are approximately the same, appearing like the results of the near analogous thermal entry problem for flow in a tube with a heated sidewall (Ref. 18).

The plotted 1800 K isotherms are approximate indications of the predicted locations of the melting interface. The extremes show that some electron condensation must occur on the side surfaces. For $\alpha = 0$ (Fig. 10A), the temperature does not even approach the melting point. On the other hand, for $\alpha = 1$ (Fig. 10D) the melting temperature is reached across the entire electrode before three-quarters of the measured length, *i.e.*, the electrode would be much shorter than the simulation. A reasonable value predicting some surface melting, and therefore tapering, appears to fall in the range of 0.1 to 0.25 for α.

Effects of Side Electron Condensation on Energy Balance

For an assumed fraction of electron condensation occurring on the side surface, the required heat transfer rate to the liquid-solid interface may be deduced by an energy balance. The experimentally measured melting rate determines the total power required. From $\rho_e(T)$ and the predicted T(x,r), the energy generation rate by resistive heating may be calculated. Integration of Equation 14 for the specified value of α gives q_{EC}, the total input due to electron condensation on the side surface. The difference then is the required heat transfer rate through the liquid drop to the liquid-solid interface at the tip,

$$q_{L\text{-}S} = \dot{m}\,\Delta H - q_G - q_{EC}$$

where ΔH represents the energy per unit mass required to melt the electrode. Figure 11 shows the predicted effects on these terms of varying α for an experiment with steel at 260 A and 2.6 cm extension.

The side surface contribution q_{EC} increases directly with α, as expected. In addition, q_G increases slightly at low values of α, and since the side heating increases the temperature locally, the electrical resistance and q_G increase. The required heat transfer rate to the interface $q_{L\text{-}S}$ drops. And for $\alpha \gtrsim 0.4$ it becomes negative. That is, in conjunction with q_G a value of $\alpha \simeq 0.4$ provides enough heating to melt the electrode entirely. Any higher value is physically unrealistic for this case. Thus, the value estimated previously, $0.1 \lesssim \alpha \lesssim 0.25$, is acceptable from the energy balance viewpoint presented in Fig. 11.

Energy Balances for Differing Materials

Energy balance analyses supplement the qualitative observations from examining temperature distributions as in Fig. 9. Predictions were made for the ranges of experimental conditions studied. Side surface electron condensation was taken as negligible ($\alpha = 0$) for each material and shielding gas, except for steel with argon ($\alpha = 0.25$). Results are summarized in Fig. 12 and generally confirm the expectations from the temperature results.

For the aluminum alloy, the resistive heating q_G is almost negligible and most of the required thermal energy flow is via the droplet to the liquid-solid interface $q_{L\text{-}S}$—Fig. 12A. For the titanium alloy, the situa-

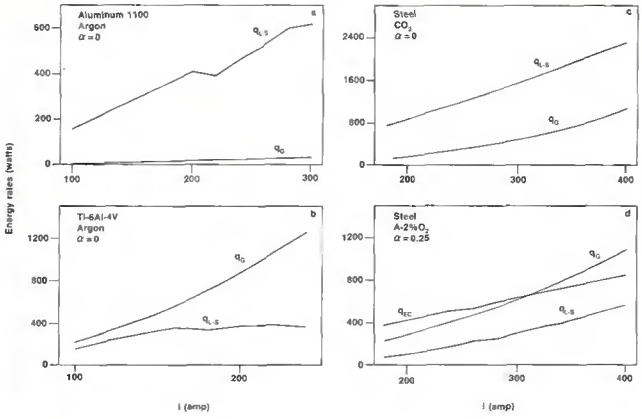

Fig. 12 – Predicted thermal energy balances for various electrode materials.

tion is partly reversed, with the majority of the required energy being provided by q_C – Fig. 12B. In both cases, the required value of q_G shows a break in its trend at intermediate currents. This break corresponds to the transition in melting rates and change from globular to spray mode of droplet detachment. These predictions emphasize the importance of the droplet behavior in the energy rate distribution, as well as weld quality.

With steel electrodes, the balance depends strongly on the shielding gas due to its effect on the electron condensation – Figs. 12C, D. With helium, predicted energy balances are comparable to carbon dioxide with slight differences in the magnitudes (Ref. 19), and about 30% of the required energy would be provided by resistive heating and the rest via the liquid-solid interface. With argon, predictions treating α as independent of electrical current show q_{EC} to be comparable in magnitude to q_C, while the required contribution of $q_{L\text{-}S}$ is reduced. Since α may vary with the surface area available to the arc at the tip of the electrode, and therefore with the electrical current, the magnitudes in this last simulation should be considered as illustrative rather than as an actual calibration. However, this comparison again demonstrates the importance of the energy contribution of electron condensation on the cylindrical side of the solid electrode, consistent with the temperature predictions and the visual observations.

An alternate explanation for the observed taper was suggested by a reviewer: the taper may be a stream of liquid from the solid electrode driven by drag from the plasma jet and electromagnetic forces. The present conduction calculations coupled with the empirical observations demonstrate that for the conditions of the experiment (moderate i and V) a uniform melting front at the end is not likely. Rather, the energy balance shows side heating is required and the temperature distributions predict that the melting isotherm is two-dimensional (tapered). The liquid then runs down this surface.

For very high currents and velocities, order-of-magnitude estimates indicate the possibility that the effects of tapering of the melting front plus high electromagnetic forces on the liquid can lead to a tapered liquid jet below the solid electrode. McEligot and Uhlman (Ref. 42) used approximations to compare capillary wave speeds to the velocity of the liquid flow, and at very high currents (*i.e.*, liquid velocities > capillary wave velocity), a liquid jet may form and then break down later into droplets. At the currents of the experiments, the capillary velocity is greater, so droplets form directly.

Concluding Remarks

Examination of typical time scales and governing parameters, experimental observations and analyses and numerical simulations of thermal conduction in moving electrodes for GMAW have led to new conclusions concerning the practicality of modeling the GMAW process. These conclusions are as follows:

1) Thermal conduction in the solid electrode may be approximated as a quasi-steady process except in the immediate vicinity of the molten droplet.

2) Dimensional and time scales analyses, including a number of the interacting transient thermal phenomena involved in droplet formation and detachment, found no significant simplification to apply in analyzing the droplet.

3) Given the transient nature of convection within the droplet, the relative significance of so many thermal phenomena and the poorly quantified boundary conditions from experiments, accurate solutions within the droplet will be very difficult.

4) In order to investigate the effects of thermocapillary convection on droplet formation and detachment, one must employ a transient analysis with provision for temporal surface deformation. A steady-state calculation for internal flow in a spherical geometry (which could be attempted with some existing general purpose codes) would be inappropriate and possibly misleading.

5) Axial thermal conduction is primarily important only for a distance of the order of 5D/Pe from the tip where it supplies the energy necessary to supplement resistive (Joule) heating and brings the temperature to the melting point.

6) Thermal conduction simulations, for steel electrodes shielded by argon gas, are quantitatively consistent with the hypothesis that electron condensation of the cylindrical side surface provides an additional energy source to form a taper at high electric currents for this combination. At 260 A, the required fraction is about 10-25%.

It is hoped that the approximate analyses presented here will provide guidance for others attempting to develop more complete models of the GMAW melting process.

Acknowledgments

The authors are grateful to the Office of Naval Research and its scientific officers, Drs. Bruce A. MacDonald, Ralph W. Judy and George R. Yoder, for encouragement, and for financial support from the Welding Science Program of their Material Science Division. Parts of the work were accomplished under financial support from the Department of Energy to Professor Eagar at Massachusetts Institute of Technology. We also thank Mssrs. Richard A. Morris and Robert R. Hardy of the David Taylor Research Center for continuous interest and advice. Mrs. Eileen Desrosiers is also to be applauded for excellent typing in a very compressed and demanding time scale.

References

1. Eagar, T. W. 1989. An iconoclast's view of the physics of welding – rethinking old ideas. *Recent Trends in Welding Science and Technology*, S. A. David and J. M. Vitek, ed., ASM, Materials Park, Ohio.

2. Lesnewich, A. 1958. Control of melting rate and metal transfer in gas shielded metal arc welding, part I – control of electrode melting rate. *Welding Journal* 37(8):343-s to 353-s.

3. Lesnewich, A. 1958. Control of melting rate and metal transfer in gas shielded metal arc welding, part II – control of metal transfer. *Welding Journal* 37(9):418-s to 425-s.

4. J. F. Lancaster, ed. 1984. *The Physics of Welding*, Pergamon Press, Oxford, England.

5. Lesnewich, A. 1987. Letter to editor, *Welding Journal* 66(12):386-s to 387-s.

6. Cooksey, C. J., and Miller, D. R. 1962. Metal transfer in gas shielded arc welding. *Physics of the Welding Arc – A Symposium 1962*, pp. 123-132.

7. Needham, J. C., and Carter, A. W. 1965. Material transfer characteristics with pulsed current. *British Welding* 12(5):229-241.

8. Greene, W. J. 1960. An analysis of transfer in gas shielded welding arcs. *Trans. AIEE* (7):194-203.

9. Halmoy, E. 1980. Wire melting rate, droplet temperature and effective anode melting

potential. *Arc Physics and Weld Pool Behavior,* Welding Institute, Cambridge, England, pp. 49–57.

10. Woods, R. A. 1980. Metal transfer in aluminum alloys. *Welding Journal* 59(2):59-s–66-s.

11. Ueguri S., Hara, K., and Komura, H. 1985. Study of metal transfer in pulsed GMA welding. *Welding Journal* 64(8):242-s to 250-s.

12. Allum, C. J. 1985. Metal transfer in arc welding as a varicose instability: I varicose instability in a current-carrying liquid cylinder with surface charge. *J. Phys. D: Appl. Phys.,* 18(7):1431–1446.

13. Allum, C. J. 1985. Metal transfer in arc welding as a varicose instability: II development of model for arc welding. *J. Phys. D: Ap pl. Phys.,* 18(7):1447–1468.

14. Waszink, J. H., and Van Den Heuvel, G. J. P. M. 1982. Heat generation and heat flow in the filler metal in GMA welding. *Welding Journal* 61(8):269-s to 282-s.

15. Waszink, J. H., and Graat, L. H. J. 1983. Experimental investigation of the forces acting on a drop of weld metal. *Welding Journal* 62(4):108-s to 116-s.

16. Waszink, J. H., and Piena, M. J. 1985. Thermal processes in covered electrodes. *Welding Journal* 64(2):37-s to 48-s.

17. Waszink, J. H., and Piena, M. J. 1986. Experimental investigation of drop detachment and drop velocity in GMAW. *Welding Journal* 65(11):289-s to 298-s.

18. Kays, W. M. 1966. *Convective Heat and Mass Transfer,* McGraw-Hill, N.Y.

19. Kim, Y.S. 1989. Metal transfer in gas metal arc welding. Ph.D. thesis, MIT, Cambridge, Mass.

20. Heiple, C. R., and Roper, J. R. 1982. Mechanism for Minor Element Effect on GTA Fusion Zone Geometry. *Welding Journal* 61(4):97-s to 102-s.

21. Oreper, G. M., Eagar, T. W., and Szekely, J. 1983. Convection in arc weld pools. *Welding Journal* 62(11):307-s to 312-s.

22. Lai, C. L., Ostrach, S., and Kamotani, Y. 1985. The role of free-surface deformation in unsteady thermocapillary flow. U.S.-Japan Heat Transfer Joint Seminar.

23. Block-Bolten, A., and Eagar, T. W. 1984. Metal vaporization from weld pools. *Met. Trans. B.* 15B(3):461–469.

24. McEligot, D. M., and Uhlman, J. S. 1988. Metal transfer in gas metal arc welding. Tech. Report, Westinghouse-0/NPT-723-HYDRO-CR-88-01, ONR Contract N000014-87-C-0668.

25. Morris, R. A. 1989. Personal communication, David Taylor Research Center, Annapolis, Md.

26. Kreith, F. 1973. *Principles of Heat Transfer,* 3rd Ed., Harper and Row, N.Y.

27. Sozou, C., and Pickering, W. M. 1975. The development of magnetohydrodynamic flow due to an electric current discharge. *J. Fluid Mech., 70* pp. 509–517.

28. Kou, S., and Wang, Y. H. 1986. Weld pool convection and its effect. *Welding Journal* 65(3):63-s to 70-s.

29. Lamb, H. 1932. *Hydrodynamics,* 6th Ed., Sec. 275, Cambridge Univ. Press.

30. Clift, R., Grace, J. R., and Weber, M. E. 1978. *Bubbles, Drops and Particles,* Academic, N.Y.

31. Pimputkar, S. M., and Ostrach, S. 1980. Transient thermocapillary flow in thin liquid layers. *Phys. Fluids,* 23(7):1281–1285.

32. Eickhoff, S.T. 1988. Gas metal arc welding in pure argon. M.S. thesis, MIT, Cambridge, Mass.

33. Allemand, C. D., Schoeder, R., Ries, D. E., and Eagar, T. W. 1985. A method of filming metal transfer in welding. *Welding Journal* 64(1):45–47.

34. Boelter, L. M. K., Cherry, V. H., Johnson, H. A., and Martinelli, R. C. 1965. *Heat Transfer Notes,* McGraw-Hill, N.Y.

35. Uhlman, J. S., and McEligot, D. M. 1989. Thermal conduction in moving electrodes. Westinghouse Naval Systems Div., Middletown, R. I., manuscript in preparation.

36. Patankar, S. V., and Spalding, D. B. 1972. A calculation procedure for heat, mass and momentum transfer in three-dimensional parabolic flows. *Int. J. Heat Mass Transfer* 15(10): 1787–1805.

37. Patankar, S. V. 1980. *Numerical Heat Transfer and Fluid Flow,* Hemisphere, Washington.

38. Rosten, H. I., Spalding, D. B., and Tatchell, D. G. 1983. *Proc. 3rd. Int. Conf. Engr. Software,* pp. 639–655.

39. Shamsundar, N., and Rooz, E. 1988. *Handbook of Numerical Heat Transfer,* W. J. Minkowyoz, *et al.,* editors, Wiley & Sons, N.Y. Chap. 18, pp. 747–786.

40. Hibbert, S. E., Markatos, N. C., and Voller, V. R. 1988. Computer simulation of moving-interface, convective, phase-change processes. *Int. J. Heat Mass Transfer,* 31(9):1785–1795.

41. Tsai, N. S. 1983. Heat distribution and weld bead geometry in arc welding. Ph.D. thesis, MIT, Cambridge, Mass.

42. McEligot, D. M., and Uhlman, J. S. 1989. Droplet formation and detachment in gas metal arc welding. Open Forum, *ASME/AIChE National Heat Transfer Conference,* Philadelphia, Pa.

Appendix

A_{cs}	Cross-sectional area
A_s	Surface area
c_p	Specific heat at constant pressure
D,d	Diameter
e	Electron charge
g	Acceleration of gravity
g_c	Unit conversion factor
H	Specific enthalpy
h	Convective heat transfer coefficient, $q_s''/(T_w - T_f)$
I	Specific internal thermal energy
i	electrical current
J	Electrical current density, i/A_{cs}
k	Thermal conductivity
L	Characteristic length, also length of electrode from contact tip to arc-molten metal interface
$\dot{m}$	Mass flow rate; melting rate
P	Period
q	Energy rate (power) or heat transfer rate; q_G, total resistive heating; q_{EC}, energy absorbed on side surfaces due to electron condensation; $q_{L\text{-}S}$, required from liquid drop to liquid-solid interface
q	Electron charge
q_G'''	Volumetric energy generation rate (resistive heating per unit volume)
q_s''	Surface heat flux
r	Radial distance; r_o, outside radius
T	Absolute temperature; T_r, reference or room temperature; T_o, amplitude of temperature fluctuations
t	Time, relative temperature (*e.g.,* °C)
u	Velocity component in axial direction
V	Voltage; V_c, apparent condensation voltage; V_a, anode voltage drop
V	Uniform or bulk velocity; V_w, electrode (wire) feed velocity
v	Velocity component in radial direction
x	Axial distance
z	Axial distance, measured from molten tip, L-x

Nondimensional Parameters

Bd, Bo	Bond numbers for thermocapillary phenomena (Lai, Ostrach and Kamotani,
Bo_d	1985 Biot number, $h \cdot Vol/lA_s \cdot k_{solid}$) Pe Peclet number, $Pr \cdot Re = Vd/\alpha$
Pr	Prandtl number, $c_p\mu/k$
Re	Reynolds number, $4\dot{m}/(\pi D\mu)$

Greek Letters

α	Fraction of total electron condensation absorbed on electrode side surface; thermal diffusivity, $k/\rho c_p$
β	Volumetric coefficient of thermal expansion
θ	Time scale; θ_T, thermal; $_v$, viscous
μ	Viscosity
υ	Kinematic viscosity, μ/ρ
ρ	Density; ρ_ℓ, liquid density
ρ_e	Electrical resistivity
σ	Surface tension; Gaussian distribution parameter
ϕ	Work function of material (volts)

Subscripts

i	Liquid-solid interface
s	Evaluated at surface conditions
w	Wire (electrode)